V Results and Discussion

Cross sections obtained in this experiment are presented and consistency among the data measured in overlapping regions of phase space is investigated. The results are compared to predictions of continuum Faddeev calculations and the implications thereof are discussed.

Differential cross sections were determined at an energy transfer ω=220 MeV for varying three-momentum transfer values q (hereafter labelled q-scan data) and at q=375 MeV/c measurements were performed over a continuous range of energy-transfer values (labelled ω-scan data). At the $(\omega, q) = (220\ \text{MeV}, 305\ \text{MeV}/c)$ kinematic setting measurements were performed over a large range of proton emission angles. Here, an extensive set of data with high statistical accuracy was collected to allow a detailed investigation of the dependence of the cross section on several observables.

5.1 Angular correlation in two-proton knockout

In the case of direct two-proton emission from ^{3}He, *i.e.*, a reaction that takes place on the proton pair and leaves the neutron as a spectator, the emission angles of the two protons are correlated by momentum conservation (as $\boldsymbol{p}'_1 + \boldsymbol{p}'_2 = \boldsymbol{q}$ at p_m=0 MeV/c). This leads to 'back-to-back' emission in the centre-of-mass frame of the virtual photon and the two protons. A larger angle of the forward proton with respect to $\boldsymbol{q}$ implies that the emission angle of the backward protons should be more forward. Therefore, such back-to-back emission is a clear signature of a direct knockout process.

This angular correlation was investigated at LQ (ω=220 MeV, q=305 MeV/c) in three different, partially overlapping, proton detector settings: LQA, LQV, and PEF (*c.f.* Table 3.2). Figure 5.1 shows a density plot of the cross section measured at LQ. The detection volume coverage extends throughout the grayed

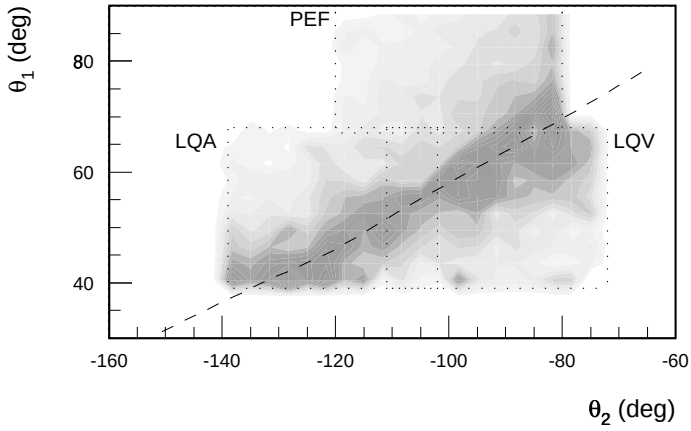

Figure 5.1: *Average experimental cross section at LQ as a function of the laboratory proton emission angles θ_1 and θ_2. The shading indicates the magnitude of the cross section, where darker shading indicates more strength (levels are not equidistant). The dashed curve indicates the angular correlation due to the back-to-back emission of the proton pair. The dotted lines indicate boundaries of the various kinematic configurations.*

area. Clearly, the larger cross sections are concentrated around the dashed curve, that corresponds to back-to-back emission of the two protons. The width of the distribution is due to the centre-of-mass motion of the neutron.

Figure 5.2 shows the differential cross section as a function of the backward proton angle for three slices in the emission angle of the forward proton. The positions of the conjugate angles, corresponding to p_m=0 MeV/c, are indicated by the arrows. The differential dV is $d\Omega_{e'}dE'd\Omega_1 d\Omega_2 dT_1$; the error bars indicate statistical uncertainties only. The overall systematic error is not indicated in the graphs and amounts to 7.4%.

Consistency checks

The data taken at q=305 MeV/c are composed of three angular settings of the HADRON detectors. This opens the possibility to verify the methods used to

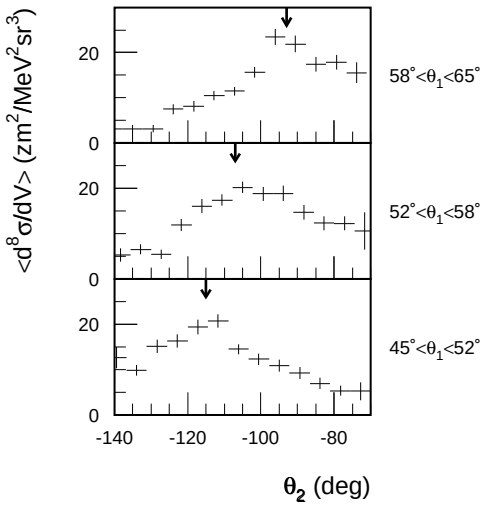

Figure 5.2: *Angular distribution of the average cross section at LQ as function of the angle of the backward proton, for three slices in the forward proton angle. The positions of the conjugate angles (see text) are indicated with arrows.*

extract cross sections from the data, by comparing the cross sections derived from different detector settings for the same region of phase space. These overlapping regions in the detection volume coverage can be identified from Fig. 5.1. The domain $40 < \theta_1 < 68°$ was covered both in LQA and LQV. The cross sections for these two settings are displayed individually in Fig. 5.3 as a function of θ_2; in the overlap region from $-111 < \theta_2 < -102°$ the ratio of the cross sections is 0.98±0.05. For the adjacent settings LQV and PEF the θ_1 distribution is shown in Fig. 5.3 for the domain $-110 < \theta_2 < -95$ °; the cross section distribution around the separation at $\theta_1 = 70°$ is continuous.

5.2 Neutron momentum distribution

For the data measured at LQ, the differential cross section is shown as a function of p_m in Fig. 5.4, averaged over the detection volume corresponding to the settings LQA and LQV, *i.e.*, $40 < \theta_1 < 68°$. The cross section decreases

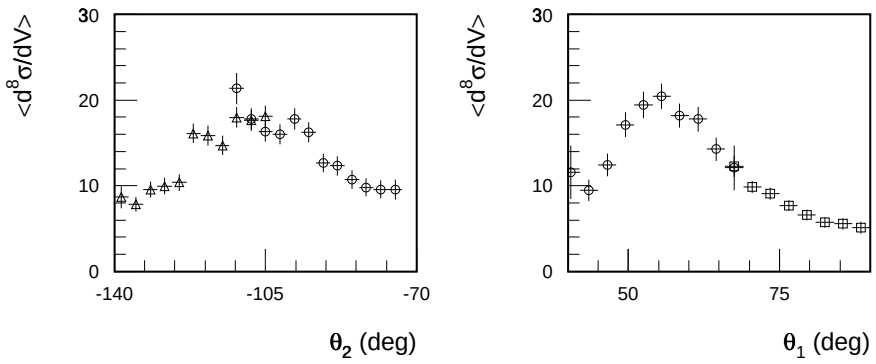

Figure 5.3: *Average cross section as a function of proton emission angles. In the left-hand panel, cross sections derived from LQA (triangles) and LQV (circles) are compared. In the right-hand panel the adjacent data sets LQV (circles) and PEF (squares) are shown. The range in the non-explicit proton angle was limited to the overlapping domain.*

roughly exponentially as a function of the neutron momentum between zero and 300 MeV/c. This reflects the neutron momentum distribution inside ^{3}He for relative momenta in the pp pair around 300 MeV/c, the region probed in this kinematic configuration (*c.f.* Fig. 2.5 and Fig. 4.14).

Signatures of two-proton knockout by one-body hadronic currents will most likely be found at low p_m – where the neutron is left approximately at rest and can be considered a spectator – since in direct pp knockout contributions from two-body currents are suppressed. Contributions from MECs are to first relativistic order prohibited as the photon will not couple to the neutral mesons exchanged in the pp pair. Additionally, the knockout via $pp \rightarrow \Delta^+ p \rightarrow pp$ is suppressed since the otherwise dominant M1 transition is forbidden by angular momentum and parity conservation rules for protons initially in a $^1S_0$ state [Wilh96].

A comparison of the data at $p_m \lesssim 100$ MeV/c with the results of continuum Faddeev calculations including only one-body currents shows a fair agreement; it accounts for approximately 50 to 80% of the measured strength in this domain, while the contribution of MECs is small (5%).

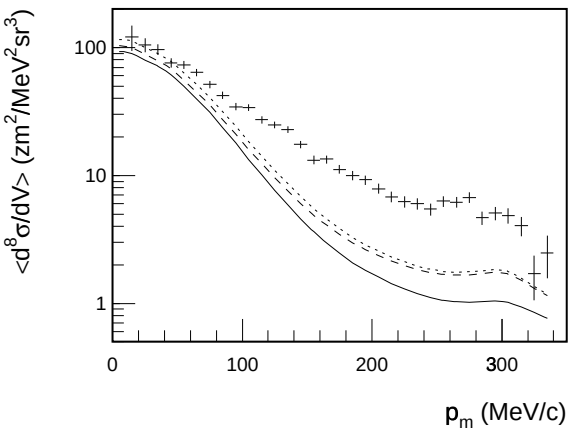

Figure 5.4: *Average cross section as a function of p_m for the combined kinematic settings LQA and LQV. The curves represent the results of continuum Faddeev calculations (solid: one-body currents only, dashed: including MECs, dotted: including MECs and static Δ currents).*

Processes at high neutron momentum

At higher missing-momentum values, one-body calculations underestimate the data by a factor of five. The high missing-momentum region is likely dominated by two-body hadronic currents (MECs and ICs), which involve coupling of the virtual photon to a proton-neutron pair. Such processes will predominantly contribute to the high p_m region in the ^{3}He$(e, e'pp)$ reaction as the momentum of the photon is shared by both nucleons involved. This expectation is supported by the results of calculations with MEC contributions, that show an increased importance of MECs of up to 40% of the calculated strength at $p_m \approx 300$ MeV/c, as compared to the low p_m region.

In the high p_m domain, also a sizeable contribution from Δ excitation can be expected. Excitation of a Δ within a pn pair, a process that is not suppressed by selection rules like in the pp case, will contribute primarily to this domain.

Moreover, excitation of the Δ resonance strongly depends on the invariant mass of the photon plus two-nucleon system. If one considers a direct reaction on

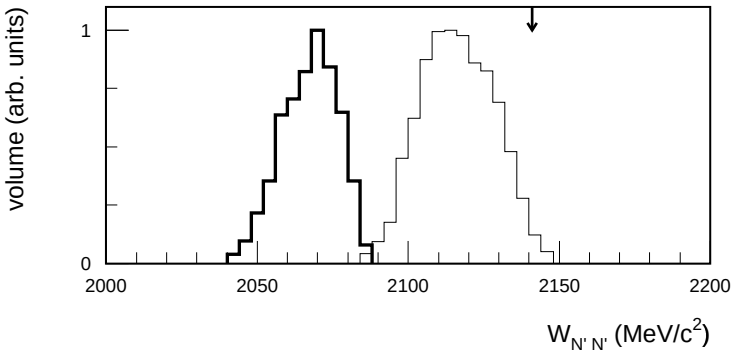

Figure 5.5: *Invariant mass of the two nucleons in the final state for the $p'_1p'_2$ pair (thick line) and the p'_1n pair (thin line) in kinematics LQ. The arrow indicates the position of the resonant peak in real-photon induced deuteron breakup [Wilh96].*

a two-proton pair, *i.e.*, at small p_m values, the invariant mass $W_{\gamma pp}$ in the initial state can be identified with the final-state observable $W_{p'_1p'_2}$. At LQ this invariant mass ranges from 2050 to 2080 MeV/c^2, which is well below the mass of the (free) ΔN system. If one assumes excitation of a pn pair, the relevant invariant energy is that of the photon plus proton-neutron system. This is reflected in the final-state quantity $W_{p'_1n'}$, which ranges from $2100 \lesssim W_{p'_1n'} \lesssim 2140$ MeV/c^2 for p_m values around 300 MeV/c (see Fig. 5.5). The invariant mass of the other pn pair, *i.e.*, $W_{p'_2n'}$, is similar to that of the pp pair for this p_m region. Therefore the cross section for intermediate Δ excitation of the p_1n pair will be dominant, since its invariant mass is closest to that of the $N\Delta$ system.

Calculations of the $^{16}\mathrm{O}(\gamma, pn)$ cross section indicate a strong dependence of the contribution of isobar currents on the photon energy, as is shown in Fig. 5.6 [Mac93]. These calculations, as well as calculations of photon-induced deuteron breakup, which use a different Δ propagator [Wilb96], indicate a maximum in the cross section due to Δ excitation around $E_\gamma \sim 250$ MeV. The equivalent invariant mass $W_{p'_1n'}$ will therefore be around 2125 MeV/c^2.

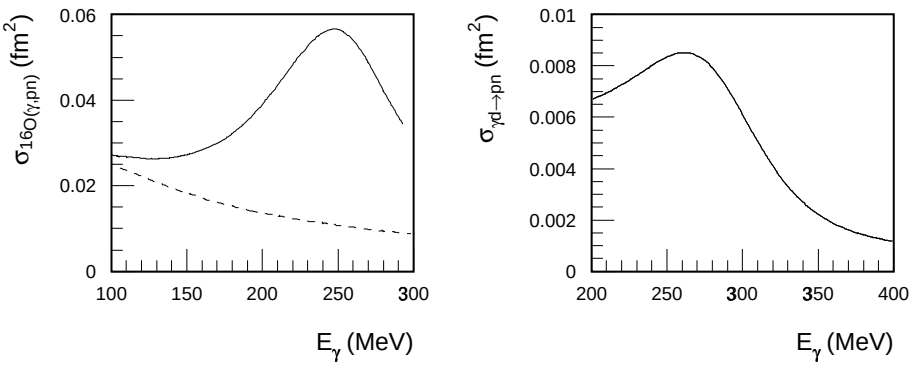

Figure 5.6: *Cross section for* $^{16}\mathrm{O}(\gamma, pn)$ *(left panel) due to MECs (dashed line) and MECs plus ICs currents (solid line) as a function of photon energy [Mac93]. The right-hand panel shows the total cross section for deuteron photodisintegration as a function of the photon energy, as calculated by Wilbois et al. [Wilb96].*

Faddeev calculations including isobar currents

Within the continuum Faddeev framework described in section 2.3, excitation of the Δ in an intermediate state was implemented within the so-called 'static' approximation. The cross sections calculated within this approximation are shown as the dotted line in Fig. 5.4: it leads to a limited (at most 5%) enhancement of the cross section, largely independent of p_m. This behaviour is not unexpected, as it has been shown that in the $^{16}\mathrm{O}(\gamma, pn)$ reaction above $E_\gamma \approx 100$ MeV [Mac93] as well as in the exclusive deuteron electro-disintegration at high momentum [Blo98], the static approach results in significantly lower cross sections compared to calculations that include a realistic (resonant) Δ propagator (see Fig. 5.7).

As of yet, no continuum Faddeev calculation is feasible that includes a realistic isobar current. The present calculations are performed in a basis built on the Jacobi momenta only in which the excitation of a Δ, requiring knowledge of the individual momenta of the nucleons, cannot be readily incorporated. This hampers a quantitative interpretation of the high p_m data obtained in this experiment.

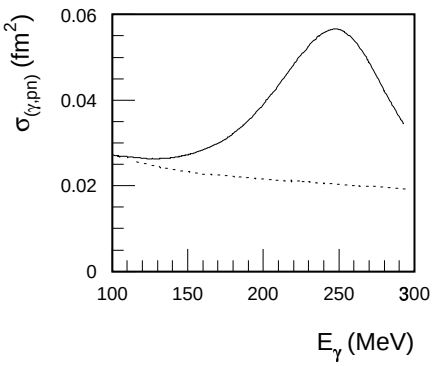

Figure 5.7: *The* $^{16}\mathrm{O}(\gamma, pn)$ *cross section for a calculation performed with a 'static'* Δ *(dotted line) and a calculation with a realistic* Δ *propagator (solid line) [Mac93].*

FSI configurations at LQ

In Fig. 5.8, the missing-momentum distributions obtained at the LQ kinematic setting are displayed for three slices in γ_1. For a fixed value of p_m the angle γ_1 implicitly fixes the kinematics of the final state, provided the direction of $\boldsymbol{p}'_2$ is kept within a limited range. For $\gamma_1 \lesssim 25°$ and $\gamma_1 \gtrsim 35°$, the three nucleons are always emitted with a sizeable momentum difference, which reduces their mutual interaction. Within the interval $25 < \gamma_1 < 35°$, a so-called 'FSI configuration' occurs. Such a configuration is characterized by two nucleons being emitted with (vectorially) similar momenta. Enhanced probability for rescattering exists between such nucleons, which may significantly influence the cross section in such domains.

In the case of LQ around 300 MeV/c, such a configuration occurs for the forward proton and the undetected neutron. Within the interval $25 < \gamma_1 < 35°$ momentum difference values p_{13} as low as 90 MeV/c are covered. This may be the origin of the 'bump' observed in the cross section around $220 \lesssim p_m \lesssim 300$ MeV/c. A similar structure is seen in the theoretical predictions, which show an enhancement of the calculated cross section with respect to the extrapolation of the exponential decay for $p_m < 200$ MeV/c.

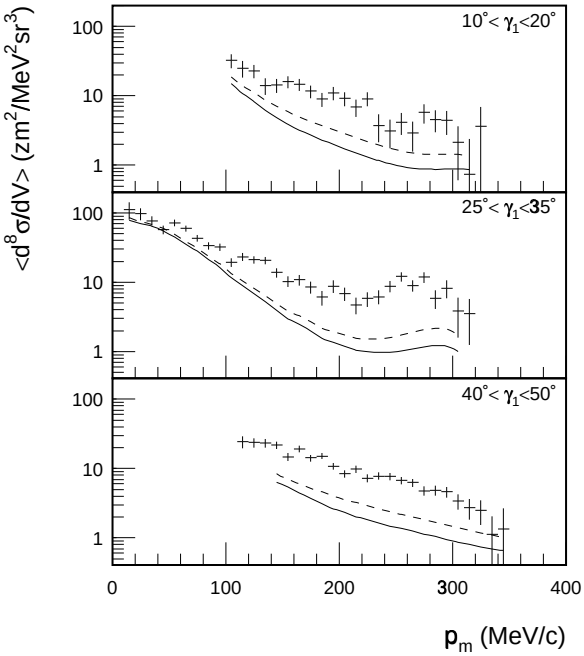

Figure 5.8: *Average cross section as a function of p_m for three slices in the forward proton angle γ_1. The solid and dashed curves represent the results of calculations with a one-body current operator and including MECs, respectively. The data were averaged over a γ_2 range from $-114°$ to $-142°$.*

5.3 FSI configurations in various kinematics

For kinematic domains in which two nucleons are emitted with similar momentum vectors, rescattering effects are an important factor that influence the cross section. Presentation of the data as a function of the momentum difference p_{ij} allows an investigation focussed on these rescattering effects.

In the HQ kinematic setting the detection volume extends to $p_{13} = 0$ MeV/c. As the cross section depends strongly on both p_{13} and p_m individually and the detection volume covered is non-rectangular in these two observables, the p_m range has to be limited to $360 < p_m < 380$ MeV/c for a proper presentation.

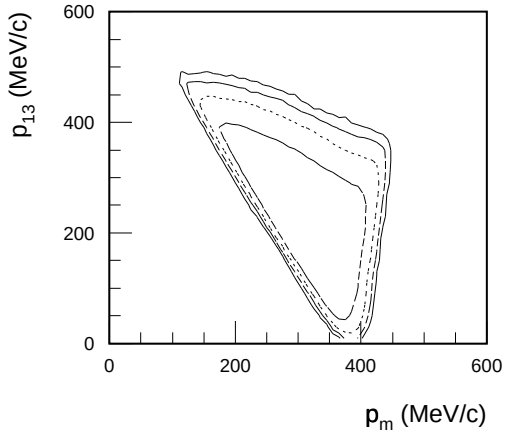

Figure 5.9: *Projection of the detection volume on the (p_{13}, p_m) plane for kinematics HQ. For detection volume coverage over the entire range $0 < p_{13} < 320$ MeV/c, the acceptance in p_m should be limited to $360 < p_m < 380$ MeV/c.*

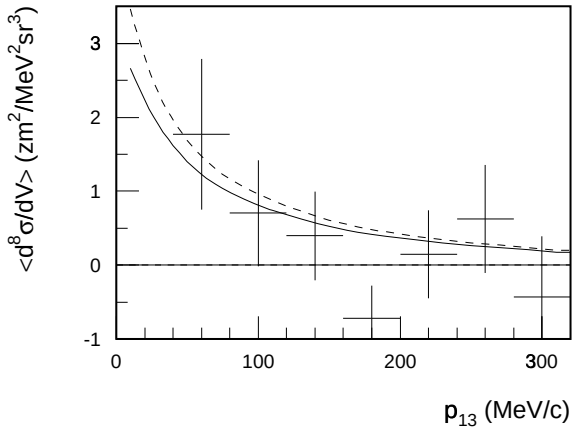

Figure 5.10: *Average cross section as a function of the momentum difference between the forward proton and the neutron for the HQ kinematic setting, for $360 < p_m < 380$ MeV/c. The solid curve represents a calculation performed with a one-body current operator, the dashed curve includes also MEC contributions.*

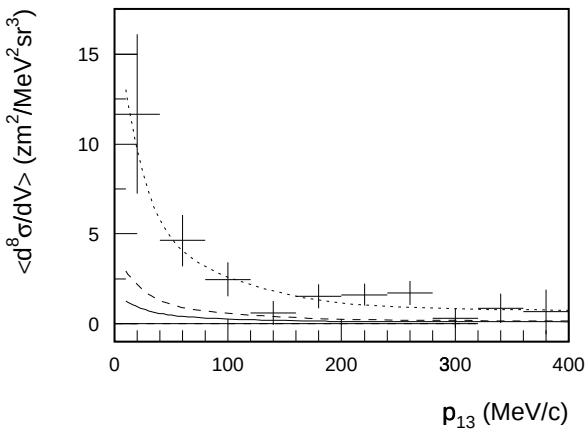

Figure 5.11: *Average cross section for the 'FSI configuration' at HW. The p_m acceptance has been limited to 360 < p_m < 410 MeV/c. The curves are results of the Faddeev calculations with a one-body current operator (solid), including MECs (dashed) and a renormalized MEC result (dotted, ×4.43).*

The shape of the detection volume is shown in Fig. 5.9. Figure 5.10 shows the average cross section for HQ for the 'FSI configuration'.

The enhancement of the cross section for $p_{13} \rightarrow 0$ MeV/c is well reproduced by the result of continuum Faddeev calculations. The statistical accuracy of the data for this p_m domain is limited, but the compatibility between the theoretical curves and the data indicates that the process of final-state rescattering is well described.

Similar configurations occur at other kinematic settings. Especially HW contains a fairly broad region in p_m – between 360 and 410 MeV/c – for which complete detection volume coverage exists at $p_{13} = 0$ MeV/c. Unfortunately, the high value of energy transfer together with the high p_m region means that a sizeable part of the reaction occurs via intermediate Δ excitation in the pn pair. The calculated cross section, including MECs, globally underestimates the data by a factor of 4.4 at $360 < p_m < 410$ MeV/c (and by a factor of 9.1 with respect to a one-body calculation) as can be seen from Fig. 5.11.

Although the absolute magnitude is not correctly predicted, the dependence of the cross section on p_{13} is well reproduced by both the one-body calculations and those including MECs. The similarity in shape between both types of calculations suggests that the shape is mainly due to NN rescattering and the absolute magnitude to the current operators used. A scaling of the calculated results, including MECs, by a factor of 4.43 results in a good agreement between data and calculations over the entire p_{13} domain. Hence, although the calculations underestimate the 'feed' into the 'FSI configuration', rescattering is correctly described by the continuum Faddeev calculations.

5.4 Varying the virtual photon characteristics

Information on the reaction mechanism and the interaction of the virtual photon with the tri-nucleon system can be obtained by varying the characteristics of the electromagnetic probe, *i.e.*, the energy transfer ω and the momentum transfer q. The data at the various (ω, q) points all show a similar dependence of the cross section on the missing momentum. This suggests an analysis of the data as a function of ω and q for slices in this final-state neutron momentum. However, also strong rescattering effects can occur at specific values of p_m, due to $p_{13} \rightarrow 0$ MeV/c, the exact position of which depends on the experimental detection volume. Therefore, no reliable comparison can be made between data for different (ω, q) settings for the p_m domain in which an 'FSI configuration' occurs. For the q-scan data, this limits the usable domain to $p_m \lesssim 220$ MeV/c, while for the ω-scan data the domain $p_m \gtrsim 300$ MeV/c should be disregarded.

Results at varying momentum transfer

In Fig. 5.12 the cross section is shown as a function of q for two slices in p_m. The data at missing-momentum values below 100 MeV/c show a decrease by a factor of four between q=305 MeV/c and q=375 MeV/c. Both this slope and the absolute magnitude of the cross sections are reasonably well described by the calculations. For both values of the momentum transfer a calculation with only one-body hadronic currents explains 72±13% of the measured strength. As expected, the inclusion of MEC contributions has only a minor effect and

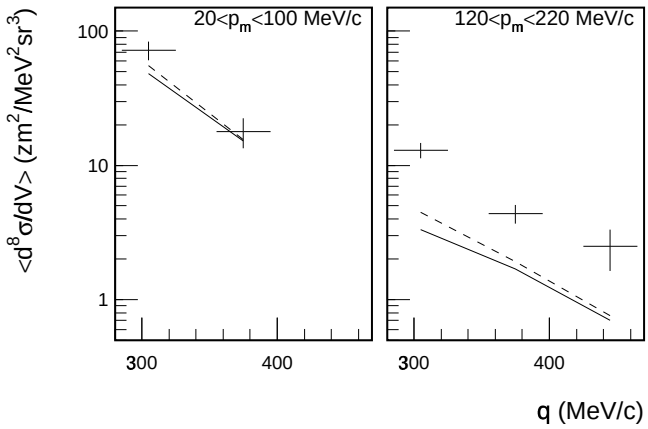

Figure 5.12: *Average cross section dependence on the momentum transfer q, for two slices in the final-state neutron momentum. The solid curves account for one-body contributions only, the dashed curves also include MECs. Data were averaged over the domain $10 < \gamma_1 < 25°$. Width of error bars indicates the range in q values covered due to the acceptance of the spectrometer. The domain $p_m < 120$ MeV/c is not covered by the detection volume of HQ.*

increases the calculated strength to 80% of the experimentally observed value. The fair agreement between data and theory for both momentum transfer values indicates that, in the p_m domain below 100 MeV/c, the cross section is predominantly driven by a one-body reaction mechanism.

In the p_m domain $120 < p_m < 220$ MeV/c, the difference between a one-body calculation and data is about a factor of five. Inclusion of MECs in the calculation increases the calculated cross section by 10 to 35%, depending on the momentum transfer, thus reducing the discrepancy to about a factor of four. The slope of data and calculations is nevertheless reasonably similar.

Results at varying energy transfer

Two-body currents, especially those involving the intermediate excitation of the Δ resonance, show a significant dependence on the invariant mass of the initial

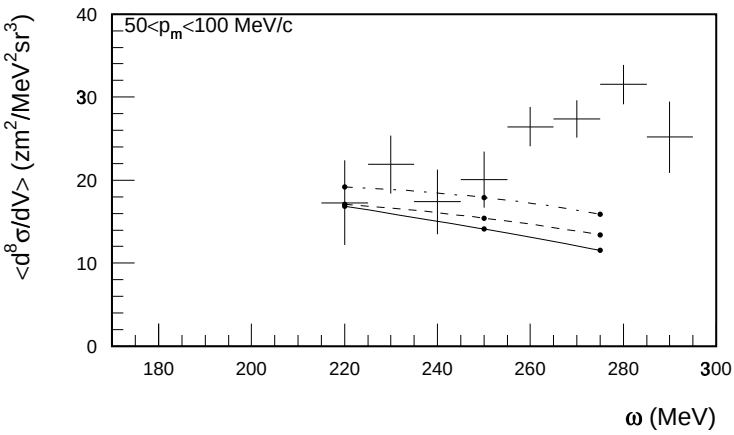

Figure 5.13: *Average cross section as a function of the energy transfer ω at q=375 MeV/c and 50 < p_m < 100 MeV/c. The curves represent calculations with a one-body current only (solid), including MECs (dashed) and including MECs and 'static' ICs (dot-dashed).*

two-nucleon plus photon system [Mac93, Wilh96]. By varying the energy transfer of the reaction the role of isobar currents can be investigated. Therefore, measurements were performed for $170 < \omega < 290$ MeV at a momentum-transfer value of q=375 MeV/c (LW, CQW, IW, and HW).

As argued in section 5.2, the low p_m region is most likely due to direct two-proton knockout, as in this domain the neutron is left 'at rest'. In case of such a direct reaction mechanism, the invariant mass of the two emitted protons $W_{p'_1 p'_2}$ can be identified with the invariant mass of the γpp system. For the ω region covered for $p_m < 100$ MeV/c, this invariant mass ranges from 2055 MeV/c^2 at $\omega = 220$ MeV (more than one full width below the peak of the Δ resonance) to 2120 MeV/c^2 at $\omega = 290$ MeV, *i.e.*, almost on top of the resonance.

In Fig. 5.13 the data for the p_m domain from 50 to 100 MeV/c at q=375 MeV/c are shown. As expected from the measurements at LQ, the agreement between data and calculations for ω=220 MeV is quite good. This already holds for a calculation with only one-body currents, which can be seen as additional evidence for the dominance of one-body currents in this p_m and ω domain.

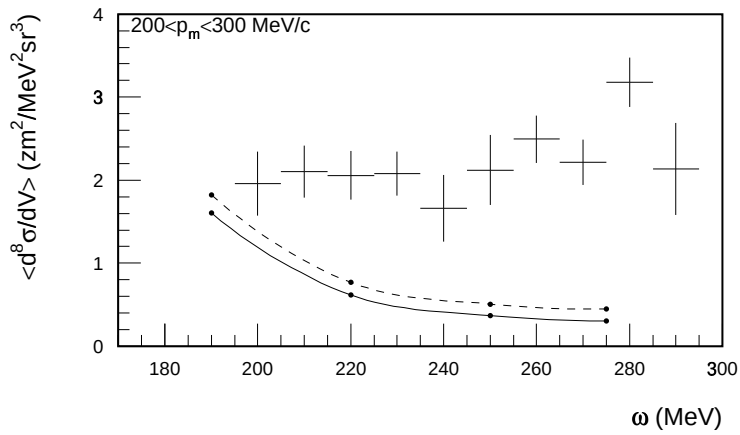

Figure 5.14: *Average cross section as a function of the energy transfer ω at q=375 MeV/c and 200 < p_m < 300 MeV/c. The curves represent calculations with a one-body current only (solid), including MECs (dashed).*

The calculations with a one-body current operator show a slightly decreasing trend as a function of ω, which is due to a changing value of the relative momentum within the *pp* pair; whereas at ω=220 MeV the central value for the relative momentum is 290 MeV/c per nucleon, it has risen to 360 MeV/c per nucleon at ω=275 MeV.

The inclusion of MECs in the calculation hardly changes the cross section at ω=220 MeV and addition of a 'static' Δ contribution changes the result by about 15%. At higher energy transfer values, the data show an increase of almost 50% over the ω range from 220 to 280 MeV. The contribution due to MECs remains rather low (below 15%). Therefore, the increase of the data probably reflects an increasing importance of intermediate Δ excitation at higher invariant masses $W_{p'_1 p'_2}$. As expected, calculations including a static approximation of the Δ current fail to reproduce this enhancement and severely underestimate the data for $\omega \gtrsim 250$ MeV.

For higher values of the missing momentum, as shown in Fig. 5.14, the measured cross section does not show any structure as a function of ω. The theo-

retical cross section calculated with a one-body current operator decreases for increasing values of ω, due to the increasing relative momentum of the protons in the pp pair. In addition, at $\omega \approx 200$ MeV, the kinematic configuration is close to an 'FSI configuration' occuring within the experimental detection volume at $p_m = 320$ MeV/c. At this low ω value, the ratio of data to theory is 1.6±0.3, whereas at higher values of the energy transfer the data overshoot theory by about a factor of ten.

In the missing momentum domain probed here, a considerable part of the strength will be due to coupling of the virtual photon to a pn pair, of which the invariant mass in the final state is considerably larger than in the γpp system: $2110 < W_{p'_1 n'} < 2190$ MeV/c^2 for $250 < p_m < 300$ MeV/c. This domain corresponds to the region where the total cross section for photon-induced deuteron breakup reaches its maximum, *i.e.*, at $E_\gamma \approx 265$ MeV [Wilh96]. This corresponds to an invariant mass of the γpn system of approximately 2140 MeV/c^2. In this energy range, the photo-induced breakup of the deuteron is known to be dominated by intermediate Δ excitation and its subsequent decay.

5.5 Signatures of the initial state

An investigation of the data at low missing momentum, *i.e.*, $p_m \lesssim 100$ MeV/c, and at an energy transfer value of ω=220 MeV, showed a dominant contribution from direct two-proton knockout by a one-body hadronic current. As argued in section 2.3, breakup induced by coupling to a one-body current in principle allows investigation of the ^{3}He bound-state wave function. Calculations indicate that the cross section is almost exclusively determined by coupling to the forward proton, and initial-state proton momentum p_1. Investigation of the cross section as a function of $p_{diff,1}$ in the low p_m domain at LQ may thus lead to insight in the initial-state wave function.

In Fig. 2.5, probabilities associated with the ^{3}He wave function were shown for various NN potentials. Within the experimentally accessible domain, the shape of the wave functions is similar for Bonn-B, CD-Bonn and Nijmegen-93. The result for Argonne v_{18} is different especially in the high p_{cm} and high p_{rel} region, but as in this domain the ^{3}He$(e, e'pp)$ cross section is not primarily driven by one-body currents no quantitative comparison with data can be made. Small

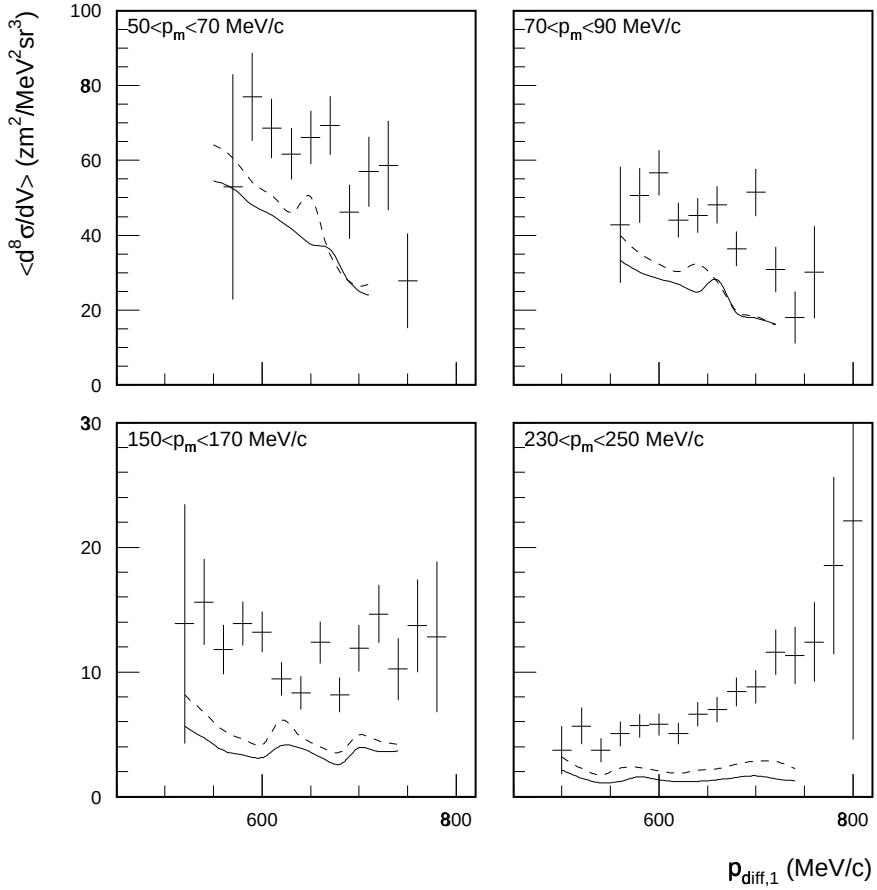

Figure 5.15: *Average cross section as a function of $p_{diff,1}$ for several slices in p_m of 20 MeV/c wide. Data are taken from the combined kinematic settings LQA, LQV and PEF. Solid curves are based on one-body currents only; dashed curves include MECs, both calculated using the Bonn-B potential. The wiggles in the calculated cross section are due to small variations in the parts of the detection volume that contribute in the different kinematic configurations.*

differences in magnitude, however, exist between the various model predictions for low p_m and here too the difference is largest for Argonne v_{18}. For all potentials one expects, based on the slope of the probability density as a function of p_{rel}, a decrease of the experimental cross section due to one-body currents as a function of $p_{diff,1}$ at low p_m, with the slope becoming increasingly more flat at higher missing momenta.

The rapid changes in cross section as a function of p_m make it necessary to investigate the $p_{diff,1}$ dependence for slices in the missing momentum, that are not wider than 20 MeV/c. In Fig. 5.15 the $p_{diff,1}$ dependence in shown for various slices of the missing momentum. The two top-graphs are adjacent slices in p_m (from 50–70 and from 70–90 MeV/c) and these already show a different slope. The fine binning thus required leads to a reduced statistical accuracy for the measured cross sections.

For the domain $p_m \lesssim 100$ MeV/c the shape of the data is fairly well reproduced by calculations performed with the Bonn-B potential. The measured slope for the region $50 < p_m < 70$ MeV/c, -0.13 ± 0.07 (zm^2/MeV^{2}sr^3) / (MeV/c), is not unlike the slope calculated including contributions due to MECs, namely -0.21 (zm^2/MeV^{2}sr^3) / (MeV/c).

At p_m values between approximately 100 and 200 MeV/c no clear structure can be observed, neither in the data nor in the calculations. However, above $p_m \approx 200$ MeV/c the data show a significant increase as a function of $p_{diff,1}$, which is not predicted by calculations. The p_m domain shown in the bottom-right panel of Fig. 5.15 is representative for the general trend above 200 MeV/c, *i.e.*, an increase by almost a factor of five between $p_{diff,1}$=600 and 800 MeV/c.

Investigation of the kinematic relations between $p_{diff,1}$ and other relevant observables for this p_m domain showed no correlation between $p_{diff,1}$ and p_{13}. It is therefore unlikely that the effect is induced by final-state rescattering. However, there is, for a fixed value of p_m, a strong correlation between $p_{diff,1}$ and the angle γ_1, as shown in Fig. 5.16.

The excitation of the Δ resonance in a pn intermediate state is expected to cause, due to its multipole character, a characteristic angular dependence of the cross section. Calculations of the coherent π^0 photoproduction cross section within the Δ-hole model [Koc83], which is dominated by the M1 multipole, show a peak around $\gamma_1^{cm} = 90°$ in the proton-plus-photon centre-of-mass sys-

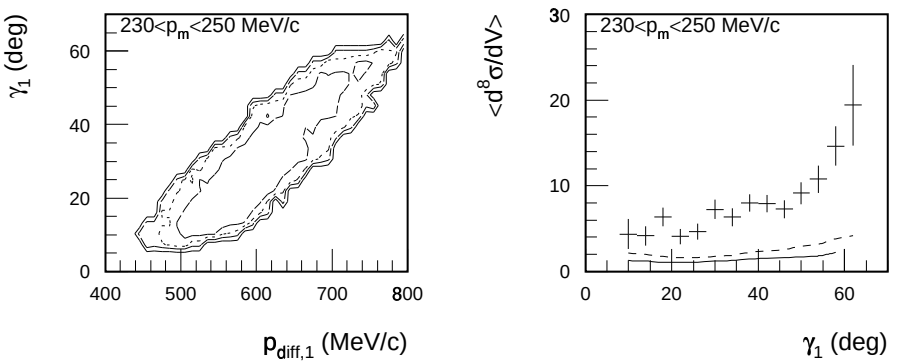

Figure 5.16: *Detection volume covered (left) by the settings LQA, LQV and PEF for the domain 230 < p_m < 250 MeV/c. In the right-hand panel the cross section is displayed as a function of γ_1 for the selected p_m interval.*

tem. Another characteristic angular dependence was found in calculations of the ^{16}O(γ, pn) cross section at $E_\gamma = 281$ MeV, a reaction that is also dominated by the Δ current [Ryc94]. The position of the resonance in this reaction varies between approximately γ_1=40° and 100°, depending on the proton energy T_1. It is therefore not unlikely that the angular dependence seen in Fig. 5.16 is induced by intermediate Δ excitation.

Comparing potential models

Figure 5.17 shows the data as a function of $p_{diff,1}$ for the same set of p_m intervals as used in Fig 5.15. Predictions based on continuum Faddeev calculations performed with different NN potential models are indicated. For the low p_m region, differences in both magnitude and slope are observed, with the Argonne v_{18} prediction being up to 15% lower than the one based on Bonn-B. In Table 5.1 the slope of the data is compared to calculations performed with a one-body current and various potential models. For the Bonn-B potential, results of calculations that include MECs are also listed.

The variations in slope between the various models are around 0.03 to 0.04. This effect is of the same order of magnitude as the effects of MECs, which was

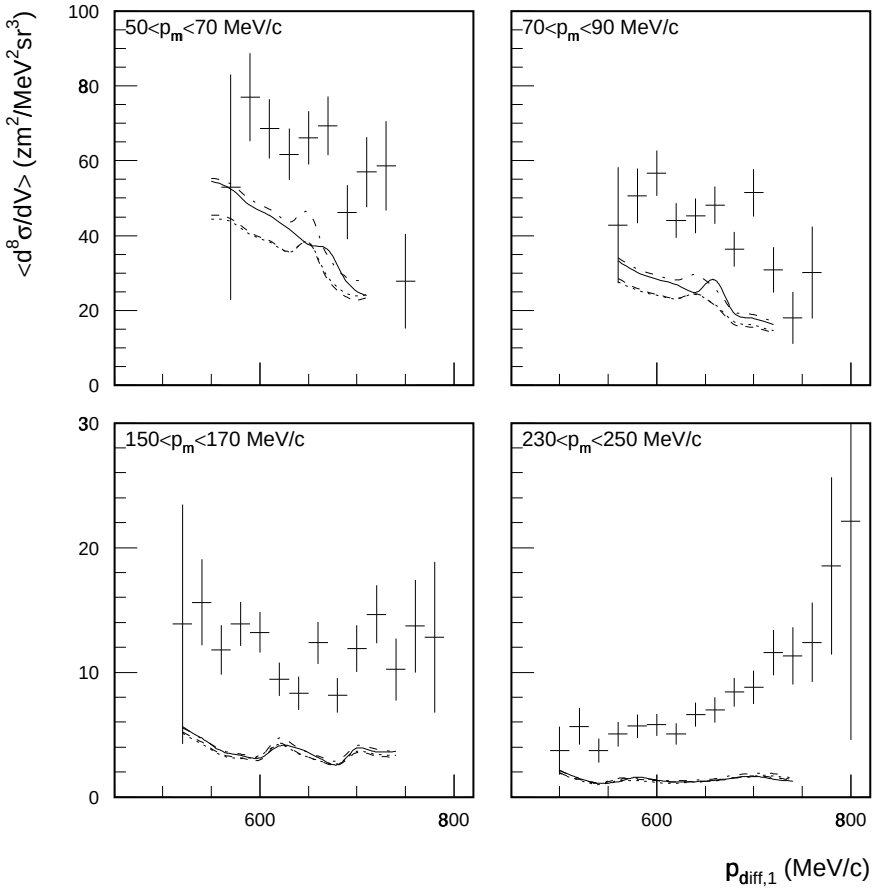

Figure 5.17: *Average cross section as a function of $p_{diff,1}$ as in Fig. 5.15. Data are compared to various potential models. Solid curve: Bonn-B, dotted: Argonne v_{18}, dashed: CD-Bonn, dot-dashed: Nijmegen-93.*

Table 5.1: *Slope of the average measured cross section as a function of $p_{diff,1}$, for two p_m intervals indicated in Fig. 5.15 and Fig. 5.17. The unit of slope is $(zm^2/MeV^2sr^3)\,/\,(MeV/c)$.*

	$50 < p_m < 70$ MeV/c		$70 < p_m < 90$ MeV/c	
Bonn-B (one-body)	-0.21		-0.11	
Argonne v_{18} (one-body)	-0.14		-0.08	
Nijmegen-93 (one-body)	-0.18		-0.11	
CD-Bonn (one-body)	-0.15		-0.09	
Bonn-B (one-body +MECs)	-0.24		-0.15	
Data	-0.13	± 0.07	-0.11	± 0.05

only calculated using the Bonn-B potential. The influence of intermediate Δ excitation on the calculated slope is as of yet unknown; also the underestimation of the data by all four calculations, which amounts to approximately 30% at $50 < p_m < 70$ MeV/c, is still not explained quantitatively. In view of these uncertainties, the low p_m data do not yet allow to express a preference for any of the potential models considered.

In the high missing-momentum region, the differences due to the NN potential are almost negligible within the experimentally probed domain. The large discrepancy between data and calculations and the unknown contribution of isobar currents hampers a quantitative comparison. Either an experimental means to isolate the isobar contribution, *e.g.*, a separation of the cross section in its structure functions, or perhaps a calculation including comprehensive treatment of Δ excitation should provide the necessary information to draw conclusions from this domain in the response.